Microtextures and crystal chemistry in $P2_1/c$ pigeonites

M. Tribaudino[1]**, D. Pasqual**[2]**, G. Molin**[2]**, and L. Secco**[2]

[1] Dipartimento di Scienze Mineralogiche e Petrologiche, Università di Torino, Torino, Italy
[2] Dipartimento di Mineralogia e Petrologia, Università di Padova, Padova, Italy

Summary

A single-crystal X-ray investigation was performed on crystals of $P2_1/c$ natural pigeonite with varying Ca and Fe* ($= Fe^{2+} + Mn^{2+}$) contents, in order to verify the effect of microtextural disorder on structure refinements and to constrain the crystal chemistry of pigeonite. Antiphase domains and exsolution lamellae affect differently the refinement results. In a crystal free of exsolution the structure obtained after refinement with all reflections is an average of that of the antiphase domains and of their boundaries, whereas in an exsolved crystal it represents only the structure of the prevailing pigeonite lamellae.

The refinement using only $h + k$ odd reflections seems to give the structure of the Ca-free pigeonite characteristic of the antiphase domains rather than that of Ca-rich domain walls. The ratio of the scale factors in refinements with all reflections and with only $h + k$ odd reflections allows the ratios of the exsolved augite and pigeonite phases to be estimated.

The crystal chemistry of the investigated samples follows the trends outlined by data on Ca-free and Fe-free synthetic samples. In particular, it is shown that Ca and Fe* substitution for Mg induce similar changes in the average structure, i.e. both induce an expansion in the M1 polyhedron and decrease the difference between the M2–O3 distances.

Introduction

Pyroxenes are a group of silicate minerals extremely common in terrestrial and extraterrestrial rocks. Articulated polymorphism and considerable isomorphic substitutions are present in pyroxenes, yielding structures with $C2/c$, $Pbca$, $P2_1/c$ and $Pbcn$ symmetries.

Among the pyroxenes, special interest has recently been paid to pigeonite, the monoclinic modification of Ca-poor pyroxene (0.05–0.20 Ca atoms per formula unit, a.p.f.u.) found in volcanic rocks and meteorites (*Pasqual* et al., 2000). Pigeonite shows two modifications, at high and low temperature, respectively: high ($C2/c$) and low ($P2_1/c$). The high–low pigeonite transformation is unquenchable, and therefore only $P2_1/c$ pigeonite is observed at room temperature.

In pigeonite, the M1 site is occupied by Mg, Fe^{2+}, Mn and the "small" cations Fe^{3+}, Al, Cr and Ti^{4+}; the M2 site is occupied by Mg, Fe^{2+}, Mn and the "large" Ca and Na ions. In low pigeonite, all structural sites are in general position, and the structure is characterized by two non-equivalent tetrahedral chains A and B, with opposite and different kinking, chain B being highly kinked and chain A more extended. After the transition to high pigeonite, these two chains become equivalent, and M1 and M2 sites are in special positions along the diad axis.

This structural complexity in pigeonite is increased by the presence – in natural but also in synthetic $P2_1/c$ pigeonite (*Fuess* et al., 1986; *Tribaudino*, 2000) – of several, often overlapping microtextures. Exsolution lamellae and mottled textures related or prior to spinodal decomposition are commonly found, due to unmixing during cooling. *Nord* and *McCallister* (1979) and *McCallister* and *Nord* (1981) have shown that mottled textures are found in samples which underwent fast cooling, whereas in conditions of slower cooling the Ca excess is exsolved as Ca-rich augite along planes parallel to (100) and/or (001). Another widespread microtexture is the occurrence of antiphase domains, due to a 1/2[110] translation related to the loss of C centering during the $C2/c \rightarrow P2_1/c$ transition in cooling. The antiphase domains are primitive and separated by C-centered antiphase boundaries. A local structure with a larger M2 polyhedron in which the Ca atoms mainly concentrate has been suggested for the boundaries (*Carpenter*, 1979). This follows from the observation that the increased size of these domains is closely controlled by Ca diffusion (*Carpenter*, 1979). Lastly, twinning (mostly on 100) has been found in pigeonites (*Toyoda* et al., 1986), perhaps related to shock events.

These microtextures can be revealed in most samples only after transmission electron microscopy (TEM) observation, since pigeonite exsolution lamellae are generally too small to be resolved by the optical microscope (*Deer* et al., 1992) and may easily be overlooked. The microtextures clearly have effects on structure refinement results. For instance, recent work has shown that increasing size in antiphase domains, obtained after prolonged annealing at high temperature, improves the quality of refinements and reduces the size of the U_{eq} of oxygen in position O3A (*Pasqual* et al., 2000). Assessment of the influence of different microtextures on refinement results enables us to interpret results critically. Several single-crystal and TEM studies have been performed on pigeonite, but as yet no investigation has been carried out on the same sample combining TEM and X-ray results. Moreover no systematic examination of pigeonite crystal chemistry has been made.

This paper aims at: 1) assessing the influence of microtextural disorder on structure refinement results; 2) investigating the crystal chemistry of pigeonite as a consequence of cation substitutions and Fe^{2+}–Mg order–disorder. Crystal-chemical and microtextural characterization of natural selected single crystals of $P2_1/c$ pigeonite ranging in composition between $Wo_6En_{76}Fs_{18}$ and $Wo_{10}En_{47}Fs_{43}$

was therefore undertaken. For $P2_1/c$ pigeonite, like *Pbca* orthopyroxene (*Ganguly* et al., 1994), Fe is considered as $Fe^{2+} + Mn^{2+}$ (indicated as Fe^*).

Experimental methods

The pigeonite single crystals chosen for this study come from the Pecora Escarpment 82506 Antarctic ureilite (PCA82506, mean composition $Wo_6En_{76}Fs_{18}$; *Toyoda* et al., 1986), Paranà (Brazil) rhyodacite BTS308 (mean composition $Wo_{10}En_{47}Fs_{43}$; *Secco* et al., 1988) and Paranà transitional basalt BTS302 (mean composition $Wo_{10}En_{57}Fs_{33}$; *Secco* et al., 1988). Data for a single crystal of composition Wo_7En_{93}, synthesized by annealing a gel of the given composition for 628 h at 1370 °C (*Tribaudino* and *Nestola*, 2002), are also discussed here, in comparison with natural crystals.

For TEM investigation samples were prepared by crushing single crystals in an agate mortar and depositing the resulting powder on a perforated carbon film. TEM studies were carried out on a CM12 Philips electron microscope operating at 120 kV.

For each sample, single crystals were then optically selected by sharp extinction and investigated by X-ray diffraction in order to identify those showing the best reflection profiles for data collection. Intensity data were collected using a Siemens AED II four-circle automated diffractometer and graphite monochromatized Mo$K\alpha$ radiation ($\lambda = 0.71073$ Å). Equivalent reflections hkl and $h\bar{k}l$ were measured in the 1.5–30° θ range using the $\omega - 2\theta$ scan mode, and subsequently merged to obtain a set of about 1000 independent reflections. Cell parameters (Table 1) were obtained by measuring the baricenter of 72 reflections collected in the 2θ angular range 18–59°, at positive and negative ω values. Further details are available in *Pasqual* et al. (2000).

After data collection, the single crystals were glued in epoxy resin and their chemical composition was determined by a CAMECA-CAMEBAX electron microprobe operating with a ~ 1 µm beam at 15 kV and 20 nA, with peak and background counting times of 20 s. Synthetic pure oxides were used as standards for Mg, Al, Ti, Cr, Mn and Fe, wollastonite for Si and Ca, and albite for Na. X-ray counts were converted to oxide weight percentages using the PAP (CAMECA) correction program. Analyses are precise to within 1% for major elements and 3–5% for minor elements. Chemical compositions (Table 2) were obtained by averaging about 20 data points for each crystal. Fe^{3+} contents were obtained by charge balance optimization, according to *Papike* et al. (1974). Further analytical details are reported in *Pasqual* et al. (2000).

Structure refinements were carried out in space group $P2_1/c$ using the SHELX-97 program, an updated version of SHELXL-93 (*Sheldrick*, 1993), taking into account all nonequivalent reflections, using F_o^2 and reflections weighted by the program according to a built-in scheme with adjustable parameters, and starting from the atomic coordinates of the Mull pigeonite described by *Morimoto* and *Güven* (1970). Totally ionized scattering curves for Mg, Fe, Mn, Al, Ti, Cr, Ca and Na, and partially ionized scattering curves for Si ($2.5+$) and O ($1.5-$) were used. Atomic scattering curves were taken from the *International Tables for X-Ray Crystallography* (*Ibers* and *Hamilton*, 1974) and *Tokonami* (1965). Structure

Table 1. *Crystal data and geometrical parameters of selected samples of pigeonite*

	PCA82506-1	BTS308-3	BTS302-3
a (Å)	9.6746(11)	9.7138(13)	9.7004(17)
b (Å)	8.8774(14)	8.9404(18)	8.9227(25)
c (Å)	5.2156(11)	5.2495(7)	5.2237(9)
β (°)	108.561(10)	108.440(10)	108.686(13)
Volume (Å^3)	424.64(12)	432.49(12)	428.30(16)
R_{int} (%)	2.07	1.30	1.95
$R1$ (%)	2.74	3.19	4.43
w$R2$ (%)	7.13	9.97	15.30
Goof	1.05	1.06	1.21
M1			
M1–O1A (Å)	2.148(1)	2.156(2)	2.159(3)
M1–O1A′ (Å)	2.040(1)	2.053(2)	2.039(4)
M1–O1B (Å)	2.173(1)	2.172(2)	2.184(3)
M1–O1B′ (Å)	2.065(1)	2.072(2)	2.072(3)
M1–O2A (Å)	2.025(1)	2.044(2)	2.039(3)
M1–O2B (Å)	2.057(1)	2.071(2)	2.068(3)
⟨M1–O⟩ (Å)	2.085(3)	2.095(4)	2.094(8)
Volume (Å^3)	11.953(4)	12.134(6)	12.109(11)
λ	1.0078	1.0074	1.0078
σ^2	23.59	22.73	23.41
M2			
M2–O1A (Å)	2.148(1)	2.172(1)	2.163(3)
M2–O1B (Å)	2.110(1)	2.144(2)	2.122(3)
M2–O2A (Å)	2.076(1)	2.083(2)	2.059(3)
M2–O2B (Å)	2.014(2)	2.044(2)	2.007(4)
M2–O3A (Å)	2.334(1)	2.441(2)	2.369(3)
M2–O3B (Å)	2.524(1)	2.643(2)	2.535(3)
⟨M2–O⟩ (Å)	2.201(3)	2.254(4)	2.209(8)
Volume (Å^3)	13.153(5)	13.776(7)	13.281(12)
SiA			
SiA–O1A (Å)	1.612(1)	1.616(1)	1.616(3)
SiA–O2A (Å)	1.593(1)	1.598(2)	1.597(3)
SiA–O3A (Å)	1.662(1)	1.659(2)	1.661(4)
SiA–O3A′ (Å)	1.644(1)	1.633(2)	1.639(3)
SiA$_{br}$ (Å)	1.653(1)	1.646(3)	1.650(5)
SiA$_{nbr}$ (Å)	1.603(1)	1.607(2)	1.607(4)
⟨SiA–O⟩ (Å)	1.628(3)	1.626(4)	1.628(7)
Volume (Å^3)	2.188(2)	2.184(2)	2.189(5)
λ	1.0080	1.0075	1.0080
σ^2	32.83	30.89	32.76
O3A–O3A–O3A (°)	163.22(1)	172.23(3)	164.64(2)
SiB			
SiB–O1B (Å)	1.620(1)	1.621(1)	1.621(3)
SiB–O2B (Å)	1.593(1)	1.597(2)	1.598(4)

(*continued*)

Table 1 (*continued*)

	PCA82506-1	BTS308-3	BTS302-3
SiB–O3B (Å)	1.671(1)	1.664(2)	1.669(4)
SiB–O3B' (Å)	1.670(1)	1.666(2)	1.669(3)
SiB$_{br}$ (Å)	1.671(1)	1.665(3)	1.669(5)
SiB$_{nbr}$ (Å)	1.606(1)	1.609(2)	1.609(5)
⟨SiB–O⟩ (Å)	1.639(3)	1.637(4)	1.639(7)
Volume (Å^3)	2.243(2)	2.236(2)	2.246(5)
λ	1.0047	1.0047	1.0047
σ^2	18.34	18.94	18.45
O3B–O3B–O3B (°)	144.26(1)	149.82(1)	144.10(1)

R_{int} internal agreement factor ($R_{int} = \Sigma|F_o^2 - \overline{F_o^2}|/\Sigma[F_o^2]$); $R1$ conventional agreement factor for reflections of $F_o > 4\sigma(R1 = \Sigma||F_o| - |F_c||/\Sigma|F_o|)$; w$R2$ weighted agreement factor for F_o^2, i.e. w$R2 = \{\Sigma[w(F_o^2 - F_c^2)^2]/\Sigma[w(F_o^2)^2]\}^{\frac{1}{2}}$; Goof = goodness of fit, i.e. Goof $= \{\Sigma[w(F_o^2 - F_c^2)^2]/(n-p)\}^{\frac{1}{2}}$, n number of reflections, p number of refined structural parameters

Table 2. *Mean electron microprobe analyses and site partitioning of the refined pigeonites*

wt%	PCA82506-1	PCA82506-3	BTS308-3	BTS308-4	BTS302-3	BTS302-4
SiO_2	55.34(20)	55.27(15)	51.12(21)	51.34(31)	51.90(32)	53.12(50)
TiO_2	0.06(2)	0.06(1)	0.31(3)	0.33(4)	0.43(3)	0.27(5)
Al_2O_3	0.65(4)	0.67(2)	0.70(3)	0.70(2)	0.74(2)	0.75(2)
Cr_2O_3	1.20(7)	1.21(6)	0.02(3)	0.01(2)	0.01(1)	0.02(3)
Fe_2O_3	–	–	0.56(23)	0.11(27)	0.36(23)	–
FeO	11.50(14)	11.88(18)	25.70(31)	26.07(23)	22.99(99)	19.38(103)
MnO	0.46(6)	0.43(4)	0.78(8)	0.78(7)	0.48(6)	0.44(5)
MgO	27.97(15)	27.77(16)	16.03(14)	16.04(14)	18.33(76)	21.21(85)
CaO	3.05(6)	3.06(4)	4.73(11)	4.65(15)	4.73(10)	4.59(8)
Na_2O	0.07(3)	0.06(2)	0.06(3)	0.06(4)	0.05(3)	0.05(2)
Total	100.30(33)	100.41(31)	100.01(50)	100.09(65)	100.02(29)	99.83(69)
Si	1.972(2)	1.970(3)	1.969(4)	1.975(6)	1.968(5)	1.978(4)
Ti	0.002(1)	0.002(0)	0.009(1)	0.010(1)	0.012(1)	0.008(1)
Al$_{tot}$	0.027(2)	0.028(1)	0.032(1)	0.032(1)	0.033(1)	0.033(1)
[4]Al	0.028	0.030	0.031	0.025	0.032	0.022
[6]Al	0.000	0.000	0.001	0.007	0.001	0.010
Cr	0.034(2)	0.034(2)	0.001(1)	–	–	0.001(1)
Fe^{3+}	–	–	0.016(7)	0.003(8)	0.010(6)	–
Fe^{2+}	0.343(4)	0.354(5)	0.828(10)	0.839(7)	0.729(34)	0.603(37)
Mn	0.014(2)	0.013(1)	0.025(3)	0.025(2)	0.015(2)	0.014(1)
Mg	1.486(5)	1.476(7)	0.920(6)	0.920(5)	1.036(39)	1.177(39)
Ca	0.116(2)	0.117(2)	0.195(4)	0.192(6)	0.192(5)	0.183(3)
Na	0.005(2)	0.004(2)	0.004(2)	0.004(3)	0.004(2)	0.004(2)
Total	3.999(2)	3.998(2)	3.999(2)	4.000(2)	3.999(2)	4.001(2)
XFe*M1	0.045	0.053	0.200	0.214	0.140	0.104
XFe*M2	0.358	0.360	0.824	0.815	0.755	0.633
XFe*tot	0.194	0.199	0.482	0.485	0.418	0.344

refinements and site occupancy determinations were performed according to the scheme outlined in *Pasqual* et al. (2000). Several crystals were refined for each sample (4 for BTS302 and PCA82506, 5 for BTS308), without significant differences in final structural parameters. Resulting structural data, bond lengths, average electron microprobe analyses and site partitioning data are listed in Tables 1 and 2 for the two best refined crystals of each sample. Observed and calculated structure-factors and atomic coordinates are available from the authors upon request.

Results and discussion

Microtextures of the refined samples

Samples PCA82506 and BTS308 are the same as those characterized by *Pasqual* et al. (2000). In some grains of sample PCA82506, irregular twinning according to (100) was found, but no exsolution texture or antiphase domains. In sample BTS308, a faint mottled texture was observed, prior to spinodal decomposition, as well as about 150 Å large, irregular and non oriented antiphase domains (*Pasqual* et al., 2000). The sample BTS308 was heated at $T = 700–1000\,^\circ C$ by *Pasqual* et al. (2000), for the calibration of the intracrystalline thermometry. Concerning microstructures, such heating induced an increase in the size of the antiphase domains up to about 2000 Å.

No exsolution textures were observed in the synthetic sample of composition Wo_7En_{93} (*Tribaudino* and *Nestola*, 2002). In addition, antiphase domains were extremely large, more than 1 μm. In sample BTS302, periodically repeated exsolution lamellae of augite within pigeonite according to (001) were observed (Fig. 1a); this orientation was confirmed by selected area diffraction patterns, showing peak splitting along the c^* axis (Fig. 1b). Streaking in the diffraction pattern along a^* and c^* suggests compositional modulation prior to further unmixing. Exsolution lamellae with different orientation, like the commonly found (100), were not observed. The periodicity of the lamellae seems to be related to size, i.e., the lower the periodicity, the larger the size. Augite lamellae vary from 100 to 500 Å and are spaced from 500 to 3000 Å. Inhomogeneous distribution of lamellar size and spacing had already been reported by *Fuess* et al. (1986) in a synthetic sample. Augite was estimated by analysis of TEM images to be present as 15% in volume. Antiphase domains of 500–2500 Å were observed in sample BTS302 (Fig. 1a), with boundaries almost normal to the exsolution plane.

Structure refinement and microtextures

The effects on structure refinement of antiphase domains and exsolution textures may be studied by comparing refinements performed using all reflections and those using only $h + k$ odd reflections (*b*-type), following the approach of *Clark* et al. (1971). The latter are only present in the primitive structure, and are expected to retain information only for pigeonitic lamellae and/or antiphase domains. Instead, diffractions with $h + k$ even have contributions from both augite and pigeonite lamellae, as well as from both domains and boundaries (*Morimoto* and *Tokonami*,
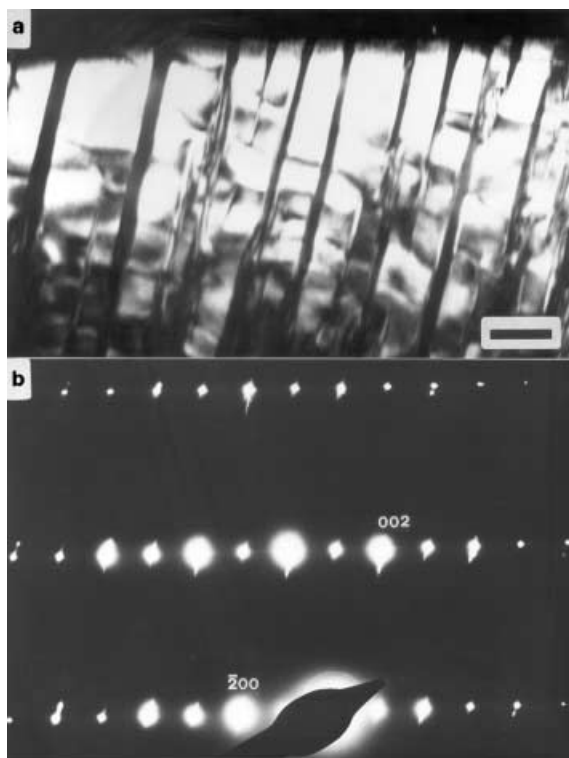
Fig. 1. **a** (001) exsolution lamellae and antiphase domains in pigeonite BTS302. Dark field image, **g** = [302]. Scale bar = 750 Å; **b** Selected area diffraction pattern of the same grain as in Fig. 1a. View along [010]

1969; *Clark* et al., 1971). In the exsolved sample BTS302, the large size of the observed antiphase domains enabled us to neglect their effects; only antiphase domains were present in sample BTS308. In the synthetic sample with composition Wo_7En_{93}, as well as in sample PCA82506, neither exsolution nor antiphase domains were expected to affect refinements significantly. It should be noted that in all the refined samples the $h + k$ odd reflections are sharp.

In sample BTS308, refinement with only $h + k$ odd reflections induced a significant decrease in displacement parameters, especially for oxygen at O3A and O3B sites, and a slight improvement in the agreement factor (Fig. 2). The size of these displacement ellipsoids in the refinement with all reflections is more than twice that obtained using only $h + k$ odd reflections, the latter being comparable with that observed in clinoenstatite (*Ohashi*, 1984). It is suggested, in agreement with *Clark* et al. (1971), that the large size of the displacement ellipsoids obtained in the refinement with all data is an effect of positional disorder. As proposed by *Carpenter* (1979) the crystal structure in $P2_1/c$ pigeonite is different at the boundaries and within the antiphase domains: the boundaries retain the high temperature $C2/c$ structure and are therefore more suitable to accept the Ca substitution. Their $C2/c$ structure allows only $h + k$ even diffrations, whereas within the domains a $P2_1/c$ structure is present allowing both $h + k$ even and odd diffractions. The structure measured with all reflections is actually an average of domains and boundaries, whereas that obtained with $h + k$ odd reflections may be referred only to the pigeonite phase within domains. This is further supported by the observation that high-temperature annealing, which increases the domain size and decreases
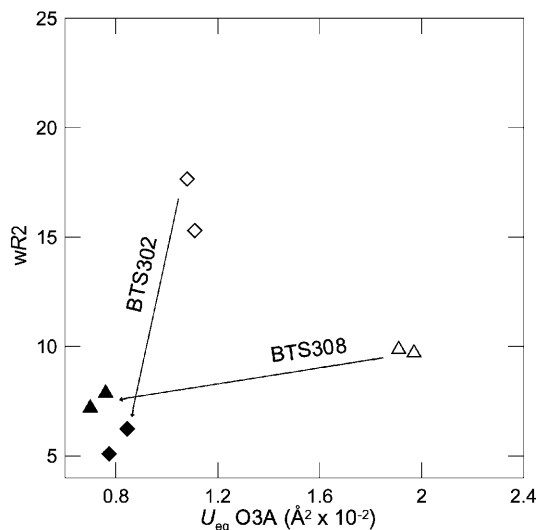
Fig. 2. Plot of w$R2$ vs U_{eq} O3A for samples BTS302 (diamonds) and BTS308 (triangles) from refinements with all reflections (empty symbols) and with only $h + k$ odd reflections (full symbols)

the boundary volume, reduces the O3A displacement ellipsoid (*Pasqual* et al., 2000).

From the above considerations the M2 polyhedral configuration of sample BTS308 from $h + k$ odd refinement gives information on the polyhedral configuration within the antiphase domains. In Table 3, M2–O bond lengths after $h + k$ odd refinement are compared for sample BTS308 with those from full data refinement and with interpolation at equal XFe*M2 $[X$Fe$^* = $ Fe$^*/($Fe$^* + $ Mg$)]$ on structural data for Ca-free $P2_1/c$ clinopyroxenes along the clinoenstatite–clinoferrosilite join (*Angel* et al., 1998): it is shown that, after $h + k$ odd refinement, M2–O3 distances (Table 3) and O3–O3–O3 angles (Fig. 3) become closer to those predicted for the Ca-free configuration. Our results confirm *Carpenter*'s (1979) suggestion that the structure of the boundaries facilitates the entry of Ca. However, there are still significant differences, indicating that some Ca is present even within the domains, contrasting with the hypotheses of *Clark* et al. (1971).

In sample BTS302, refinement performed using only $h + k$ odd reflections led to a dramatic drop in the agreement factors, confirming that the low quality of results is due to exsolution in this sample, as $h + k$ odd reflections come only from pigeonite lamellae and $h + k$ even reflections result from the superimposition, at least partial, of augite and pigeonite contributions (Fig. 2, Table 3). The observed difference in the agreement factors is due to strong residuals (up to 2.1 e$^-$), present in the full data refinement, close to almost every atom, and not present in the other refined samples. These residuals disappear in refinements using $h + k$ odd reflections. They are therefore interpreted to correspond to the contribution of augite lamellae, which was neglected in the refinement process.

In Table 3 the polyhedral configuration of M2 is compared for BTS302 also in refinements with all and $h + k$ odd reflections. In contrast to sample BTS308 only minor changes in bond lengths and in the size of the displacement parameters for the O3 atoms are found in the $h + k$ odd refinements (Table 3, Figs. 2 and 3); it is therefore suggested that the structural results of the refinement with all data mainly concern those of the pigeonite lamellae. The presence of strong residuals

Table 3. M2–O bond lengths, chain kinking angles, U_{eq}O3A and wR2 ($wR2 = \sqrt{\Sigma[w(F_o^2 - F_c^2)^2]/\Sigma[w(F_o^2)^2]}$) for BTS308, BTS302 and PCA82506, after the refinements with only $h + k$ odd and with all reflections, averaged among the refined crystals for each sample. In round brackets the average of the experimental standard deviation, in square brackets the standard deviation for the average of the values in all the refined crystals (4 for BTS302 and PCA82506, 5 for BTS308). M2–O bond lengths for a fictive Ca-free clinopyroxene of the same XFe*M2 as in the BTS308 sample is given, from a fit of Angel et al. (1998) structural data. Data for Wo7En93 from Tribaudino and Nestola (2002); refinements with $h + k$ odd reflections were performed specifically for this study

|	Wo7En93		BTS308			BTS302		PCA82506	
	All reflections	$h + k$ odd only	Fictive Ca-free	All reflections	$h + k$ odd only	All reflections	$h + k$ odd only	All reflections	$h + k$ odd only
M2–O1A (Å)	2.125(1)	2.132(4)	2.156	2.171(1) [1]	2.175(20) [23]	2.164(3) [2]	2.164(12) [3]	2.147(2) [1]	2.142(21) [19]
M2–O1B (Å)	2.096(1)	2.104(4)	2.115	2.144(2) [1]	2.153(21) [25]	2.120(4) [1]	2.116(12) [5]	2.111(2) [2]	2.108(21) [14]
M2–O2A (Å)	2.081(1)	2.060(3)	2.034	2.082(2) [2]	2.021(14) [9]	2.060(4) [1]	2.064(9) [15]	2.077(2) [3]	2.069(13) [26]
M2–O2B (Å)	2.004(1)	2.001(3)	1.982	2.043(2) [2]	1.980(14) [6]	2.009(4) [3]	2.018(8) [21]	2.015(2) [1]	2.014(13) [21]
M2–O3A (Å)	2.299(1)	2.291(2)	2.405	2.440(2) [4]	2.405(4) [4]	2.364(4) [5]	2.364(3) [5]	2.335(2) [3]	2.328(6) [3]
M2–O3B (Å)	2.490(1)	2.482(2)	2.549	2.642(2) [4]	2.577(4) [3]	2.529(4) [5]	2.506(2) [6]	2.524(2) [4]	2.509(6) [5]
M2–O3A (Å)	3.609(1)	3.604(3)	3.629	3.423(2) [8]	3.492(4) [6]	3.585(4) [3]	3.608(2) [5]	3.573(2) [4]	3.579(5) [6]
M2–O3B (Å)	3.051(1)	3.043(3)	3.097	2.947(2) [4]	2.986(5) [2]	3.040(4) [2]	3.062(3) [5]	3.030(2) [3]	3.036(6) [6]
O3A–O3A–O3A (°)	160.6(1)	160.4(2)	165	172.1(1) [3]	169.2(1) [2]	164.6(1) [3]	164.0(1) [2]	163.3(1) [2]	162.8(1) [1]
O3B–O3B–O3B (°)	143.0(1)	142.8(2)	142	149.8(1) [2]	147.0(1) [1]	143.9(1) [2]	143.0(1) [1]	144.2(1) [2]	143.5(1) [2]
U_{eq}O3A(Å$^2 \times 10^{-2}$)	0.91(3)	0.89(6)	–	1.98(4) [6]	0.70(7) [8]	1.20(7) [17]	0.88(10) [15]	1.35(4) [21]	1.11(6) [22]
wR2(%)	8.6	8.4	–	10.6 [1.3]	7.9 [7]	18.2 [2.3]	6.3 [1.0]	11.2 [4.1]	9.3 [3.6]
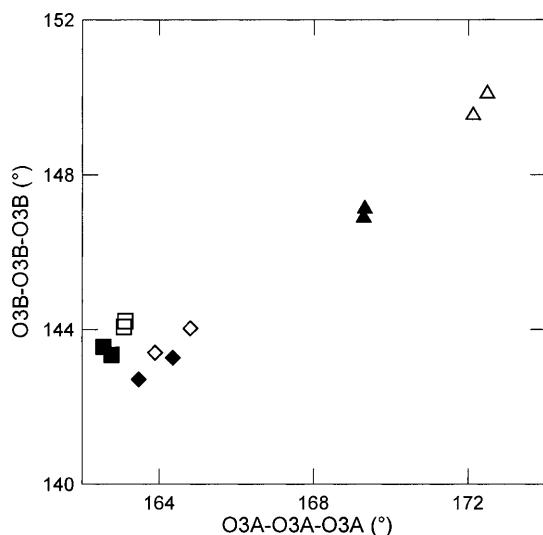
Fig. 3. O3B–O3B–O3B vs O3A–O3A–O3A chain angles resulting from refinements with all reflections (empty symbols) and with $h + k$ odd reflections only (full symbols). Squares, diamonds and triangles: samples PCA82506, BTS302 and BTS308, respectively

indicates that appreciable contribution to the intensity of $h + k$ even reflections by exsolved augite on (001) significantly affects refinement.

Lastly, for samples PCA82506 and Wo_7En_{93}, with large antiphase domains and no exsolutions, refinements with all reflections and with only $h + k$ odd reflections yielded almost the same M2 polyhedral bond lengths (Table 3), with no significant decrease in the size of O3 displacement parameters or in the agreement factor. These results confirm that the above observed differences in refinements with different set of reflections are indeed due to an effect of microstructures.

Exsolution lamellar volume

The relative amount of the primitive phase in sample BTS302 may be estimated from the ratio of the observed scale factors in refinements with and without $h + k$ even reflections, as in *Clark* et al. (1971). Volumes of primitive lamellae between 84.2 and 85.8% were observed in the four refined crystals, with remarkable agreement, both internally and with TEM observations. In orthopyroxenes, the ratio of augite vs. orthopyroxene was estimated by the intensity of reflections forbidden to the *Pbca* space group, ascribed to the contribution of $C2/c$ augite lamellae (*Domeneghetti* et al., 1995). In a subsequent paper, the same authors (*Domeneghetti* et al., 1996) showed that this ratio could be refined, with significant improvements in the quality of results. However, an attempt to refine the augite vs. pigeonite ratio in our exsolved pigeonite failed. There are in fact two significant differences between this and the case of orthopyroxene: 1) no absolute scaling of the $C2/c$ phase was possible, as its reflections completely or nearly overlap those of $P2_1/c$ (apart from $0k0$ with k odd reflections, which are in any case extremely faint); 2) the orientation of the augite and pigeonite reciprocal lattice is in higher offset than in the case of augite and orthopyroxene (Fig. 1b, this work; Fig. 2 in *Domeneghetti* et al., 1995). Further investigations, perhaps by means of area detectors, would be required for optimum data correction.

Reliability of refinements with only $h + k$ odd reflections

The reliability of structural refinements performed with only $h + k$ odd reflections may be questioned, as they are generally weaker and are expected to be measured less precisely. This results in lower precision in structural results, shown by higher standard deviations. In order to verify the possible presence of false minima, structural refinement tests were performed by changing the starting coordinates and including or excluding different sets of reflections. In the different refinements for a given structural parameter convergence was achieved at very similar values, always within 2σ. In addition, the M2–O3 distances, which are very important in determining the effect of Ca in the M2 polyhedral configuration, showed the lowest standard deviations and the best internal agreement in refinements performed with only $h + k$ odd reflections. The O3 atoms, which show a larger deviation from a unique C-centered pseudosymmetric position, were in fact better determined by refinement with $h + k$ odd reflections than other atoms. These results confirm recent findings from leverage analysis of XRD data from pigeonite (*Merli* et al., unpublished), which indicate that $h + k$ odd reflections have a great influence on determining atomic positions of M1, M2, O3A and O3B sites.

Average crystal chemistry

Tetrahedral chains and M1 polyhedron

In analogy with *Pbca* orthopyroxene (*Domeneghetti* et al., 1985), changes in octahedral layer configuration induce some important effects on the tetrahedral arrangement – mainly straightening of the O3–O3–O3 kinking angle along the c axis. This observed straightening is induced by increasing both Ca occupancy at M2 and by total Fe* contents (*Ohashi* and *Finger*, 1976; *Domeneghetti* et al., 1985; *Angel* et al., 1998). In our samples, chain kinking angles increase by 9° and 6° in chains A and B, respectively, between samples PCA82506 and BTS308, as the latter is Ca- and Fe*-richer (Fig. 3). Chain A straightening along the [001] direction is higher than that of chain B, due to the smaller size of the SiA with respect to the SiB tetrahedra (Table 1): as the M1 polyhedron increases in size with increasing Fe* content, the tetrahedral chain rotates to compensate for the increase, and the SiA tetrahedra must undergo higher rotation to achieve an increment along **c** equivalent to that of the SiB tetrahedron.

Figure 4 shows the M1 polyhedral volume vs. refined Fe* contents for the samples studied in this work and for synthetic samples. The data of this work fall above the synthetic Ca-free trend. Comparisons with the Wo_7En_{93} Fe-free sample along the diopside–enstatite join indicate that this is due to the effect of higher Ca contents in our pigeonites, further confirmed by the observation that structure refinements performed on a crystal of sample BTS308 after annealing at high temperature outline a trend parallel to that for synthetic samples. It therefore appears that Ca, although it does not enter the M1 site, indirectly affects the size of the M1 polyhedron. A similar feature was observed by *Angel* et al. (1989) in the $(Cr, Mg)MgSi_2O_6$ pyroxene, for which (although only Mg is present in the M1 site) the size of M1 is much greater than that found in clinoenstatite, as an effect of cation substitution at the M2 site.
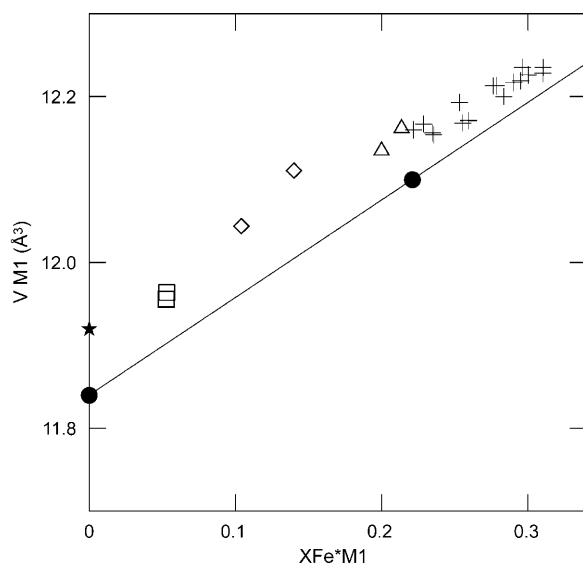
Fig. 4. Variation of the M1 polyhedral volume with the site occupancy of $X\text{Fe}^*\text{M1}$. Data for Ca-free enstatite–ferrosilite join (*Angel* et al., 1998, full circles), Fe-free synthetic clinopyroxene of composition $\text{Wo}_7\text{En}_{93}$ (*Tribaudino* and *Nestola*, 2002, full star) and refinements of sample BTS308 after heating for intracrystalline thermometry calibration (*Pasqual* et al., 2000, crosses). Other symbols as in Fig. 3

M2 polyhedron

Like the M1 polyhedron, changes in M2 individual bond lengths may be interpreted as effects of combined $\text{Mg}-\text{Fe}^{2+}$ and Ca substitutions, mainly influencing M2–O3A and M2–O3B bond lengths, as shown in Fig. 5a–d. Increases in these bond lengths are visible in synthetic, natural, and natural heated samples with respect to Fe^{2+} and Ca substitutions for Mg. The samples studied here have longer bond distances than synthetic Ca-free ones, due to the increasing size of the M2 polyhedron. The exsolved samples from BTS302 are peculiar in that their average structure – mainly as regards the M2–O3 bond lengths, which are longer and reveal more changes – falls close to the trend outlined by Ca-free samples, although the average chemical analysis indicates Ca contents of about 0.18 Ca a.p.f.u. (Table 2). As discussed above, this may be an effect of the exsolved nature of our samples. The Ca content of the pigeonite exsolution is probably much lower: the analytical value is the average of two exsolved phases whereas the structure obtained from refinements is close to that of the pigeonite fraction.

Ca generally induces an increase in all bond lengths within coordination, whereas Fe^* does not increase M2–O2A and M2–O2B bond lengths. Both Fe^* and Ca decrease the bond lengths of M2 with out-of-coordination O3A and O3B oxygens, which become coordinated in the $C2/c$ structure of Ca-rich clinopyroxenes. An overall decrease in the difference between the M2–O3A and M2–O3B couples, which become unique in the $C2/c$ structure, is observed with increasing Fe^* and Ca (Fig. 5); both substitutions therefore point to a $C2/c$ structure. For Ca in Fe-free samples, this occurs at 0.6 Ca a.p.f.u. (*Tribaudino*, 2000), whereas for
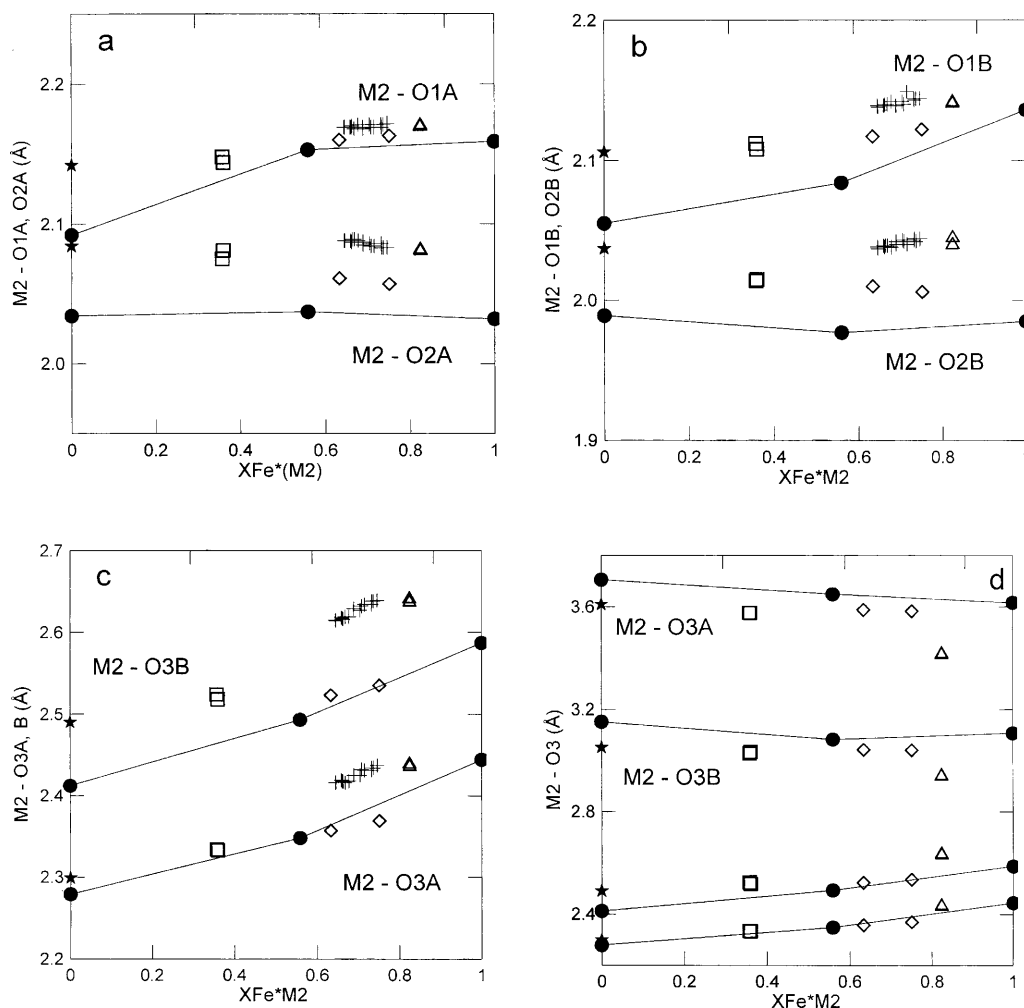
Fig. 5. M2–O bond distances vs XFe*M2. **a** M2–O1A and M2–O2A; **b** M2–O1B and M2–O2B; **c** M2–O3A and M2–O3B; **d** M2–O3, also including the out of coordination M2–O3A and M2–O3B bond distances; the two unnamed trends refer to the shorter M2–O3A and M2–O3B distances. Symbols as in Fig. 4

Ca-free pyroxenes a $P2_1/c$ structure is always retained, even in clinoferrosilite. However, in Fe-rich samples, the transformation to $C2/c$ was reached with lower Ca contents (0.4 Ca a.p.f.u. along the hedenbergite–ferrosilite join; *Ohashi* et al., 1975).

Cell parameters

Figure 6 shows cell parameters for refined samples vs. total XFe*, compared with the trend reported by *Angel* et al. (1998) for synthetic Ca-free samples. Increases in parameters *a*, *b* and *c* with Fe* contents and of parameters *a* and *c* with increasing Ca are observed, in both synthetic samples and those studied here. These changes follow established trends discussed, among others, by *Angel* et al. (1998): the Ca in M2 and total Fe* increase the size of octahedral interstratification, thus increasing
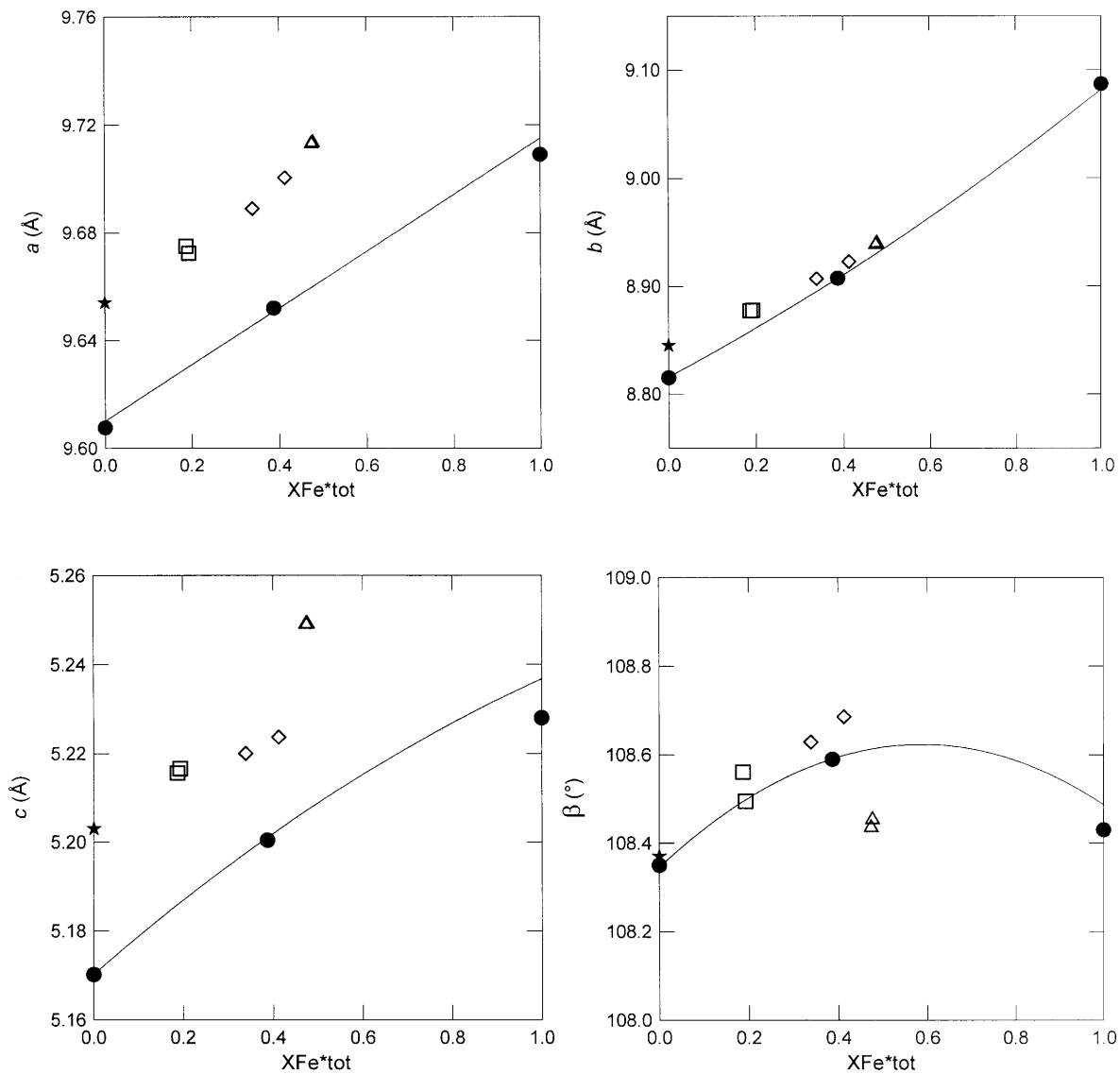
Fig. 6. Cell parameters vs XFe*tot. Symbols as in Fig. 4. The trend from the synthetic data in *Angel* et al. (1998) is shown

parameter a, whereas the higher expansion on the c axis is probably related to the increase in kinking angles of both A and B chains, due to Ca and Fe* substitutions.

Conversely, the behavior of the β angle is not regular; the effect of Fe* changes with increasing contents, with an inversion at about 0.5 XFe*tot, as discussed in *Angel* et al. (1998).

Acknowledgments

References

Angel RJ, Gasparik T, Finger LW (1989) Crystal structure of a Cr^{2+}-bearing pyroxene. Am Mineral 74: 599–603

Angel RJ, McCammon C, Woodland AB (1998) Structure, ordering and cation interactions in Ca-free $P2_1/c$ clinopyroxenes. Phys Chem Mineral 25: 249–258

Carpenter MA (1979) Experimental coarsening of antiphase domains in a silicate mineral. Science 206: 681–683

Clark JR, Ross M, Appleman DE (1971) Crystal chemistry of a lunar pigeonite. Am Mineral 56: 888–908

Deer WA, Howie RA, Zussman J (1992) An introduction to the rock-forming minerals, 2nd ed. Longman, London

Domeneghetti MC, Molin GM, Tazzoli V (1985) Crystal-chemical implications of the Mg^{2+}–Fe^{2+} distribution in orthopyroxenes. Am Mineral 70: 987–995

Domeneghetti MC, Molin GM, Stimpfl M, Tribaudino M (1995) Orthopyroxene from the Serra de Magé meteorite: structure refinement and estimation of $C2/c$ pyroxene contributions to apparent *Pbca* diffraction violations. Am Mineral 80: 923–929

Domeneghetti MC, Tazzoli V, Boffa Ballaran T, Molin GM (1996) Orthopyroxene from the Serra de Magé meteorite: a structure-refinement procedure for a *Pbca* phase coexisting with a $C2/c$ exsolved phase. Am Mineral 81: 842–846

Fuess H, Schröpfer L, Feuer H (1986) Exsolution and phase transformations in synthetic pyroxenes: X-ray and TEM studies at elevated temperatures. Ber Bunsen Phys Chem 90: 755–759

Ganguly J, Yang H, Ghose S (1994) Thermal history of mesosiderites: constraints from compositional zoning and Fe–Mg ordering in orthopyroxenes. Geochim Cosmochim Acta 58: 2711–2723

Ibers JA, Hamilton WC (eds) (1974) International tables for X-ray crystallography, 4. Kynoch Press, Birmingham, pp 99–101

McCallister RH, Nord GL Jr (1981) Subcalcic diopsides from kimberlites: chemistry, exsolution microstructures, and thermal history. Contrib Mineral Petrol 78: 118–125

Morimoto N, Güven N (1970) Refinement of the crystal structure of pigeonite. Am Mineral 55: 1195–1209

Morimoto N, Tokonami M (1969) Domain structure of pigeonite and clinoenstatite. Am Mineral 54: 725–740

Nord GL, McCallister RH (1979) Kinetics and mechanism of decomposition in $Wo_{25}En_{31}Fs_{44}$ clinopyroxene. Geol Soc Am, Abstracts with Programs 11: 488

Ohashi Y (1984) Polysynthetically-twinned structures of enstatite and wollastonite. Phys Chem Mineral 10: 217–229

Ohashi Y, Finger LW (1976) The effect of Ca substitution on the structure of clinoenstatite. Carn Inst Wash Year Book 75: 743–746

Ohashi Y, Burnham CW, Finger LW (1975) The effect of Ca–Fe substitution on the clino-pyroxene crystal structure. Am Mineral 60: 423–434

Papike JJ, Cameron KL, Baldwin K (1974) Amphiboles and pyroxenes: characterization of other than quadrilateral components and estimates of ferric iron from microprobe data. Geol Soc Am, Abstracts with Programs 6: 1053–1054

Pasqual D, Molin G, Tribaudino M (2000) Single-crystal thermometric calibration of Fe–Mg order–disorder in pigeonites. Am Mineral 85: 953–962

Secco L, Carbonin S, Dal Negro A, Mellini M, Piccirillo EM (1988) Crystal chemistry of pyroxenes from basalts and rhyodacites of the Paranà basin (Brazil). In: *Piccirillo EM, Melfi AJ* (eds) The mesozoic flood of the Paranà Basin: petrogenetic and geophysical aspects. São Paulo University, Brazil, 600 p

Sheldrick GM (1993) Shelxl-93. Program for crystal structure refinement. Göttingen University, Germany

Tokonami M (1965) Atomic scattering factor for O^{2-}. Acta Cryst 19: 486

Toyoda H, Haga N, Tachikawa O, Takeda H, Ishii T (1986) Thermal history of ureilite, Pecora Escarpment 82506 deduced from cation distribution and diffusion profile of minerals. Proceedings, 10th Symposium on Antarctic Meteorites, pp 206–221

Tribaudino M (2000) A transmission electron microscope investigation on the $C2/c$–$P2_1/c$ phase transition in clinopyroxenes along the diopside–enstatite ($CaMgSi_2O_6$–$Mg_2Si_2O_6$) join. Am Mineral 85: 707–715

Tribaudino M, Nestola F (2002) Average and local structure in $P2_1/c$ clinopyroxenes along the join diopside–enstatite ($CaMgSi_2O_6$–$Mg_2Si_2O_6$). Eur J Mineral 14 (in press)

Authors' addresses: *M. Tribaudino* (corresponding author), Dipartimento di Scienze Mineralogiche e Petrologiche, Università di Torino, Via Valperga Caluso 35, I-10125 Torino, Italy, e-mail: triba@dsmp.unito.it; *D. Pasqual*, *G. M. Molin*, and *L. Secco*, Dipartimento di Mineralogia e Petrologia, Università di Padova, Corso Garibaldi 37, I-35127 Padova, Italy, e-mail: daria@dmp.unipd.it, gmario@dmp.unipd.it, luciano@dmp.unipd.it